


ARTICLE

Open Access

Boosting ion dynamics through superwetable leaf-like film based on porous $g\text{-C}_3\text{N}_4$ nanosheets for ionogel supercapacitors

Minjie Shi¹, Cheng Yang¹, Chao Yan¹, Jintian Jiang¹, Yongchao Liu¹, Zhenyu Sun², Weilong Shi¹, Gang Jian¹, Zhanhu Guo³ and Jong-Hyun Ahn⁴ 

Abstract

Ionic liquid (IL) electrolytes have enormous potential for the development of high energy density supercapacitors (SCs) owing to their wide potential windows, but ILs are plagued by sluggish ionic diffusion due to their high viscosity and large ion size. Exploiting superwetable electrodes possessing high compatibility with IL electrolytes remains challenging. Inspired by the biological characteristics observed in nature, a unique film electrode with a *Monstera* leaf-like nanostructure is synthesized and used to overcome the aforementioned bottleneck. Similar to the pores in *Monstera* leaves that allow the permeation of air and water vapor, the film electrode is based on porous $g\text{-C}_3\text{N}_4$ nanosheets (~ 1 nm thick) as ion-accessible “highway” channels, allowing ultrafast diffusion of IL ions. The film exhibits a high diffusion coefficient ($3.68 \times 10^{-10} \text{ m}^2 \text{ s}^{-1}$), low activation energy ($0.078 \text{ mJ mol}^{-1}$) and extraordinary wettability in the IL electrolyte, indicating its superior IL ion dynamics. As a proof of concept, flexible ionogel SCs (FISCs) with tailorability and editability are fabricated, which exhibit a high energy density (10.5 mWh cm^{-3}), high-power density, remarkable rate capability, and long-term durability, outperforming previously reported FISCs. Importantly, these FISCs can be effectively charged by harvesting sustainable power sources, particularly the rarely studied wind power, for practical applications.

Introduction

With the rapid development of portable and wearable electronics, developing lightweight, reliable, and flexible energy-storage devices is a critical challenge^{1,2}. Supercapacitors (SCs), owing to their fast charge/discharge capability and almost unlimited lifetime, have been considered promising energy-storage devices to supply power for various electronic devices^{3–5}. Because the energy density of SCs is proportional to the square of the working voltage, the amount of energy stored in SCs mainly depends on the stability of the applied electrolyte over the

voltage range^{6–8}. Owing to their wide potential window ($>2.5 \text{ V}$), nonvolatility, nonflammability, and high thermal/chemical stability, flexible ionogel SCs (FISCs) based on ionic liquid (IL) electrolytes not only have great promise for achieving a high energy density but are also safe and have a wide usage temperature range in portable and wearable electronics⁹. Nevertheless, the large ion size and high viscosity of IL electrolytes always lead to poor compatibility with the electrode, resulting in sluggish ionic diffusion, which affects the electrochemical kinetics of FISCs^{10,11}. Accordingly, it is important to design a novel electrode with a suitable structure for the development of high-performance FISCs.

In nature, many plants have numerous small pores (also known as “stomata”) in their leaves, e.g., *Monstera* leaves. These pores are important to the physiology of plants because they provide accessible channels for air and water

Correspondence: Chao Yan (chaoyan@just.edu.cn) or Zhenyu Sun (sunzy@mail.buct.edu.cn) or Jong-Hyun Ahn (ahnj@yonsei.ac.kr)

¹School of Materials Science and Engineering, Jiangsu University of Science and Technology, 212003 Zhenjiang, China

²State Key Laboratory of Organic-Inorganic Composites, Beijing University of Chemical Technology, 100029 Beijing, China

Full list of author information is available at the end of the article.

© The Author(s) 2019



Open Access This article is licensed under a Creative Commons Attribution 4.0 International License, which permits use, sharing, adaptation, distribution and reproduction in any medium or format, as long as you give appropriate credit to the original author(s) and the source, provide a link to the Creative Commons license, and indicate if changes were made. The images or other third party material in this article are included in the article's Creative Commons license, unless indicated otherwise in a credit line to the material. If material is not included in the article's Creative Commons license and your intended use is not permitted by statutory regulation or exceeds the permitted use, you will need to obtain permission directly from the copyright holder. To view a copy of this license, visit <http://creativecommons.org/licenses/by/4.0/>.

vapor during photosynthesis and cellular respiration. Inspired by this biological characteristic, an effective approach is to fabricate electrodes with a well-developed porous structure to provide numerous accessible channels and a short diffusion distance for electrolyte ions¹². As a novel porous material, graphitic carbon nitride nanosheets (*g*-C₃N₄ NSs) can be facilely synthesized on a large scale with low cost and exhibit an abundant, continuous, and adjustable porous structure^{13–15}. In contrast to most porous materials, *g*-C₃N₄ NSs with ultrathin walls do not suffer from the inner-pore ion-transfer kinetics problem^{12,16}. Additionally, the natural structure of *g*-C₃N₄ NSs includes a large number of pyrrolic N “hole” defects in the lattice and doubly bonded N at the edges of the vacancy, which are beneficial for the adsorption and motion of electrolyte ions^{13,17,18}.

Extensive research has focused on directly growing or depositing pseudocapacitive materials on *g*-C₃N₄ NSs as SC electrodes^{19,20}. For example, Zhang et al. constructed a lamellar Ni–Al double hydroxide/*g*-C₃N₄ NS hybrid electrode via an in situ self-assembly approach²¹ that delivered a specific capacitance as high as 714 F g⁻¹ at 0.5 A g⁻¹. Zhao et al. prepared a TiO₂/*g*-C₃N₄ NS hybrid electrode with improved specific capacitance and no loss after 1000 cycles in SCs²². However, it is challenging to obtain a flexible SC electrode based on *g*-C₃N₄ NS hybrids owing to their inadequate mechanical properties and electrical conductivity²³. It has been demonstrated that the incorporation of carbon nanotubes (CNTs) provides long continuous conductive paths and mechanical stability of the electrode for flexible energy-storage devices^{24,25}. Conductive CNTs, which are characterized by a high aspect ratio and efficient assembly with other nanomaterials, particularly various nanosheets, contribute to the formation of robust three-dimensional (3D) interconnected architectures^{26–28}. Nevertheless, neither the integration of *g*-C₃N₄ NSs with CNTs for flexible electrodes and their application in FISCs nor the investigation of *g*-C₃N₄ NSs as accessible channels for IL electrolyte ions has been reported.

In this work, a film electrode (MCNN/CNT) with a bioinspired *Monstera* leaf-like nanostructure is proposed and was fabricated by growing MnO₂ nanoparticles on porous *g*-C₃N₄ NSs embedded in a CNT network. Owing to the porous *g*-C₃N₄ NSs as ion-accessible channels, the film electrode exhibited favorable ion dynamics and superior wettability in the IL electrolyte. Furthermore, the 3D architecture supported by porous *g*-C₃N₄ NSs and conductive CNTs ensured mechanical stability and charge transport. As a proof of concept, a prototype of these tailorable FISCs was fabricated and exhibited a high energy/power density and remarkable rate and cycling performance, outperforming previously reported FISCs.

FISCs can be charged by harvesting solar/wind energy and can effectively power various portable electronics.

Materials and methods

Material detailed information

Multiwalled CNTs with high purity were purchased from Chengdu Organic Chemicals Co., Ltd., Chinese Academy of Sciences. The diameter and length of the CNTs are 10 nm and 20 μm, respectively. 1-Ethyl-3-methylimidazolium tetrafluoroborate (EMIMBF₄) IL was obtained from the Center for Green Chemistry and Catalysis, Lanzhou Institute of Chemical Physics, Chinese Academy of Sciences. EMIMBF₄ IL was vacuum-dried at 100 °C overnight before use. All chemical reagents used in this study are of analytical grade and used without further purification.

Synthesis of *g*-C₃N₄ NSs

Bulk *g*-C₃N₄ was prepared via the direct thermal polycondensation of melamine as follows: 5 g of melamine powder was placed into an alumina crucible with a cover and heated to 520 °C for 2 h at a heating rate of 5 °C min⁻¹. The yellow bulk *g*-C₃N₄ was vigorously milled into a powder using a mortar. Next, 1 g of bulk *g*-C₃N₄ was uniformly spread into an alumina ark with dimensions of 60 × 30 × 20 mm to ensure good contact between bulk *g*-C₃N₄ and air and was then heated to and maintained at 550 °C in an open system for 2 h at a heating rate of 10 °C min⁻¹. Subsequently, the light-yellow powder was heated at 520 °C for 1 h in air at a heating rate of 20 °C min⁻¹. Finally, porous *g*-C₃N₄ NSs (yield ~50 mg) were obtained as the resulting white powder (Fig. S1a).

Preparation of MCNNs/CNTs film

First, 12 mg of *g*-C₃N₄ NSs powder was added to 50 mL of deionized water with sonication for 5 min. Then, 20 mL of a 0.02-M KMnO₄ solution and 20 mL of a 0.03-M MnSO₄·4H₂O solution were slowly added with stirring for 3 h. The resultant MCNN composite was collected via centrifugation, washed, and dispersed into deionized water to form a homogeneous MCNN solution. Then, the treated CNT aqueous dispersion (additional details are presented in Fig. S4) was mixed with the MCNN solution with continuous stirring for 20 h. The mass ratio of MCNNs to CNTs was approximately 60:40. Finally, the mixture solution was vacuum filtered through a cellulose ester filter membrane (pore size of 0.22 μm) and then peeled from the membrane to obtain the MCNN/CNT film (~1.65 g cm⁻³). For comparison, a similar process was employed for the preparation of an MnO₂/CNT film without *g*-C₃N₄ NSs. Moreover, further experiments were conducted on growing MnO₂ on a mixture of CNTs and *g*-C₃N₄ NSs (Fig. S18).

Assembly of FISCs

The resultant MCNN/CNT and CCNN/CNT films (additional details are presented in Fig. S8) were used as positive and negative electrodes, respectively. First, each film electrode (2 cm × 3 cm) was glued to a Ni slice using conducting Ag paste. Then, the ionogel electrolyte was slowly sandwiched between two film electrodes, which were pressed together under a pressure of ~1 MPa for 30 min. After the assembly, the FISCs were dried under vacuum at room temperature and stored in an Ar-filled glovebox for testing. The ionogel electrolyte was prepared as follows. First, 0.6 g of poly(vinylidene fluoride-hexafluoropropylene) (P(VDF-HFP)) was dissolved in an acetone solution. Then, 1.8 g of EMIMBF₄ IL was added to the resulting solution under stirring until the solution became clear. EMIMBF₄ was the IL electrolyte used in our research. EMIMBF₄ is a relatively cheap and readily available IL electrolyte that is widely used as an electrolyte in energy-storage devices. The resulting viscous solution was cast onto a glass Petri dish to evaporate the acetone for 1 h to obtain the ionogel electrolyte.

Characterization

Field-emission scanning electron microscopy (SEM, FEI Sirion 200) and transmission electron microscopy (TEM, JEM-2100F) were carried out to characterize the morphology of the samples. Atomic force microscopy (AFM) images were recorded on a MultiMode 8 (Bruker) in ScanAsyst mode. X-ray diffraction (XRD) patterns were characterized on a powder XRD system with Cu K α radiation, and X-ray photoelectron spectroscopy (XPS) measurements were performed on a Kratos AXIS Ultra DLD spectrometer with an Al K α X-ray source. Nitrogen absorption and desorption measurements were performed with an Autosorb IQ instrument at 77 K. The specific surface area was calculated using the Brunauer–Emmett–Teller method, and the pore-size distribution was determined from the adsorption branch of the isotherm according to density functional theory. The surface tension of the EMIMBF₄ IL was tested using a surface tensiometer (K100, Germany). The wettability of the films in the IL was measured using a contact angle measuring instrument (DCA300, Germany). The surface free energy of the films was determined using the two-liquid-phase method.

Electrochemical measurements

All electrochemical tests were performed using a VMP3 multifunctional electrochemical analysis instrument (Bio-Logic, France) via cyclic voltammetry (CV), galvanostatic charge–discharge (GCD), and electrochemical impedance spectroscopy (EIS) methods. The CV and GCD tests were performed at various scan rates

and current densities. The EIS measurements were performed in the frequency range of 0.01 Hz to 100 kHz. The volumetric specific capacitance, energy density, and power density of the FISCs were calculated using the galvanostatic discharge curve, according to the two-electrode systematic calculation method:

$$C = (I \times \Delta t) / (\nu \times \Delta U), \quad (1)$$

$$E = C \times (\Delta U)^2 / 7.2, \quad (2)$$

$$P = 3600 \times E / \Delta t, \quad (3)$$

where C (F cm⁻³) is the volumetric specific capacitance, E (mWh cm⁻³) is the volumetric energy density, P (mW cm⁻³) is the volumetric power density, I is the discharge current, Δt is the discharge time, ΔU is the voltage variation during the discharge process after the “IR drop”, and ν (cm³) is the total volume of the FISC (including the two film electrodes and the ionogel electrolyte). Additionally, the electrochemical kinetic behaviors of the MCNN/CNT and MnO₂/CNT film electrodes in the EMIMBF₄ IL electrolyte were compared using the three-electrode systematic method.

Results and discussion

As schematically shown in Fig. 1a, MCNN/CNT film electrodes were prepared through vacuum filtration via the solution-phase assembly of MCNNs and CNTs, yielding MnO₂ nanoparticles grown on *g*-C₃N₄ NSs to form MCNNs and then embedded in a highly purified CNT network. The TEM image (Fig. 1b) showed a two-dimensional lamellar morphology with abundant pores on the layers of the *g*-C₃N₄ NSs. These pores were open and continuous, and an ultrathin pore wall was observed (Fig. 1c). The ultrathin wall could reduce the inner-pore migration distance of the electrolyte ions. According to the AFM image, the thickness of the *g*-C₃N₄ NSs was ~1 nm (Fig. 1d), further indicating the efficient exfoliation process of *g*-C₃N₄ NSs. Figure 1e shows the TEM image of the MCNN/CNT film electrode; spherical MnO₂ nanoparticles ranging from 50 to 100 nm in size were tightly anchored on the *g*-C₃N₄ NSs, and both were entrapped in the CNT matrix. The interconnective porous *g*-C₃N₄ NSs and conductive CNTs in the film electrode jointly served as the backbone, mimicking the Monstera leaf with abundant pores and veins (inset in Fig. 1e). A cross-sectional SEM image (Fig. 1f) revealed that the average thickness of the MCNN/CNT film electrode was ~40 μ m. A magnified image (Fig. 1g) indicated that the well-distributed MCNNs were homogeneously embedded in the CNT network, forming a 3D architecture. The robust skeleton ensured the high mechanical stability of the

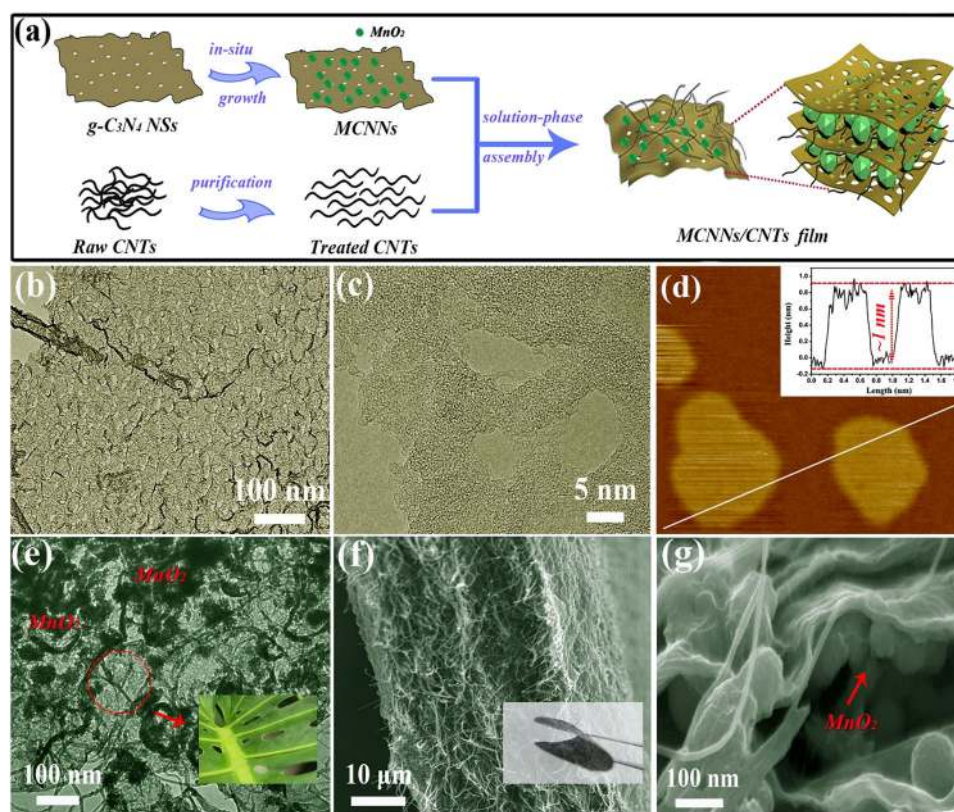


Fig. 1 Synthesis process and morphology characterizations. **a** Schematic showing the fabrication process and architectural features of the MCNN/CNT film. **b** TEM, **c** high-resolution TEM, and **d** AFM images of $g\text{-C}_3\text{N}_4$ NSs. **e** TEM image of the MCNN/CNT film. The inset in **e** shows the structure of the MCNN/CNT film, which was inspired by the Monstera leaf. **f** Low- and **g** high-magnification cross-sectional SEM images of the MCNN/CNT film. The inset in **f** shows a digital photo of a flexible MCNN/CNT film electrode

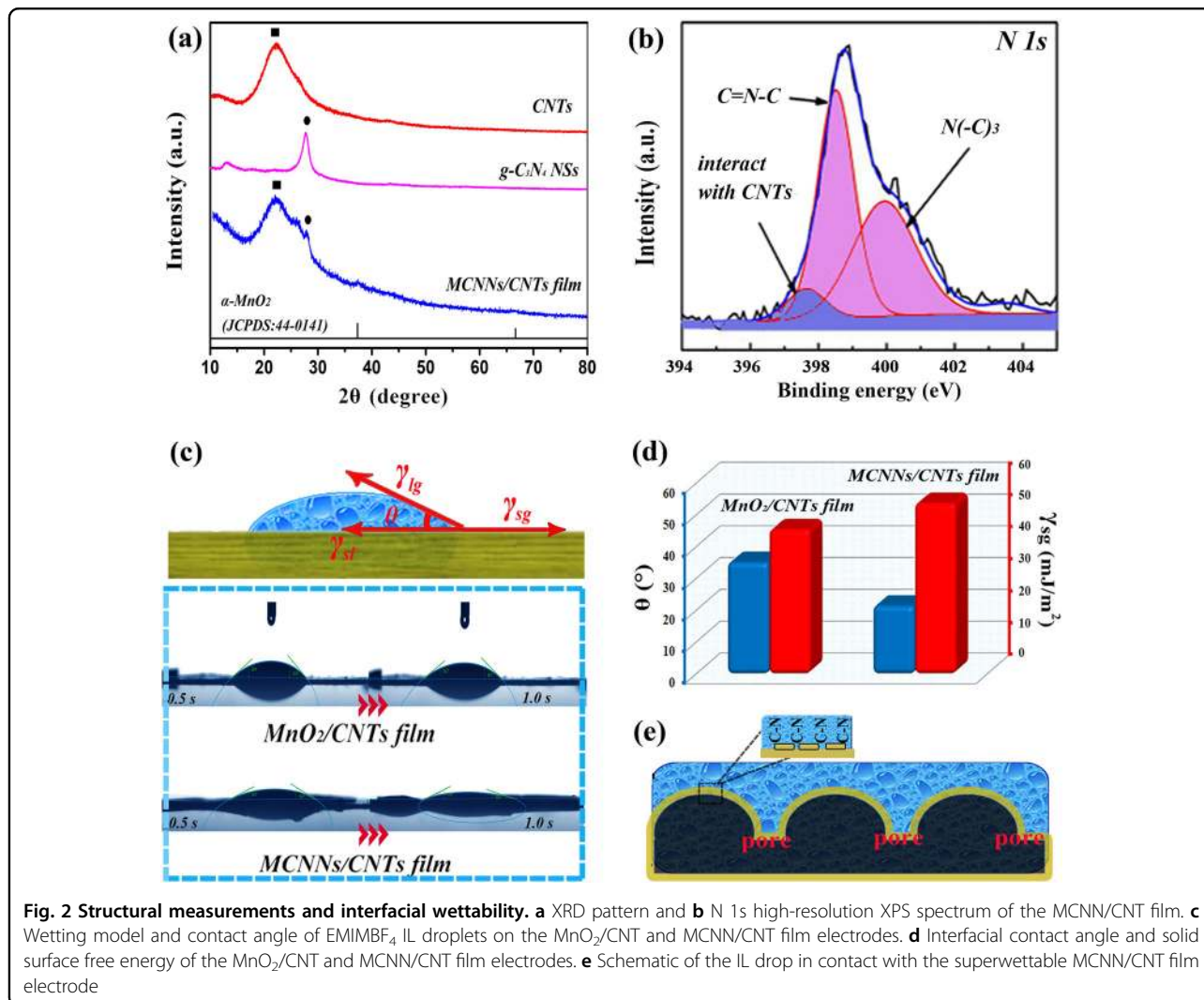
MCNN/CNT film electrode (inset in Fig. 1f). More information regarding the morphology and structure analyses of $g\text{-C}_3\text{N}_4$ NSs, CNTs, and MCNNs is provided in the Supporting Information (Fig. S1–S4).

Figure 2a shows the XRD patterns of CNTs, $g\text{-C}_3\text{N}_4$ NSs, and MCNN/CNT film. Apart from the peak at 27.6° corresponding to the (002) diffraction plane of the $g\text{-C}_3\text{N}_4$ NSs and 25.6° corresponding to the (002) diffraction plane of the CNTs, there were two weak diffraction peaks at $\sim 37.8^\circ$ and 67.1° in the XRD pattern of the MCNN/CNT film (Fig. 2a), which were indexed to $\alpha\text{-MnO}_2\cdot\text{H}_2\text{O}$ (JCPDS No. 44–0141) with low crystallinity. More information about MnO_2 in MCNNs is provided in Fig. S3. As shown in Fig. 2b, the XPS high-resolution N 1s spectrum indicated three N species. The dominant peaks at 399.8 and 398.3 eV could be assigned to the bridging N atoms in $\text{N}(\text{C})_3$ and the sp^2 -bonded N atoms in the triazine rings ($\text{C}-\text{N}=\text{C}$) of the $g\text{-C}_3\text{N}_4$ NSs, and the shoulder peak at 397.6 eV was due to the strong interaction between the CNTs and the N atoms in the $g\text{-C}_3\text{N}_4$ NSs^{29,30}, confirming the robust self-assembly of the CNTs and MCNNs in the MCNN/CNT film

electrode. Wettability is one of the most crucial properties of a film electrode^{10,31–33}. For a droplet of liquid on a flat solid surface, the wetting behavior is determined by Young's equation^{34,35}:

$$\gamma_{sl} = \gamma_{sg} - \gamma_{lg} \times \cos \theta. \quad (4)$$

There is a relationship among the contact angle (θ), the surface tension (γ_{lg}) of the liquid, the surface free energy (γ_{sg}) of the solid, and the interfacial free energy (γ_{sl}) between the solid and liquid. Figure 2c shows the wetting process of the EMIMBF₄ IL drop in contact with the MnO_2/CNT and MCNN/CNT film electrodes. The MCNN/CNT film electrode was almost completely wetted by the IL electrolyte, exhibiting significantly better wettability than the MnO_2/CNT film electrode. The small θ (18.4°) and large γ_{sg} (50.2 mJ m^{-2}) of the MCNN/CNT film electrode in the IL electrolyte (Fig. 2d) confirmed its excellent wettability. The γ_{lg} of the EMIMBF₄ IL electrolyte was measured to be $\sim 52.4 \text{ mJ m}^{-2}$, and the γ_{sl} of the MCNN/CNT film



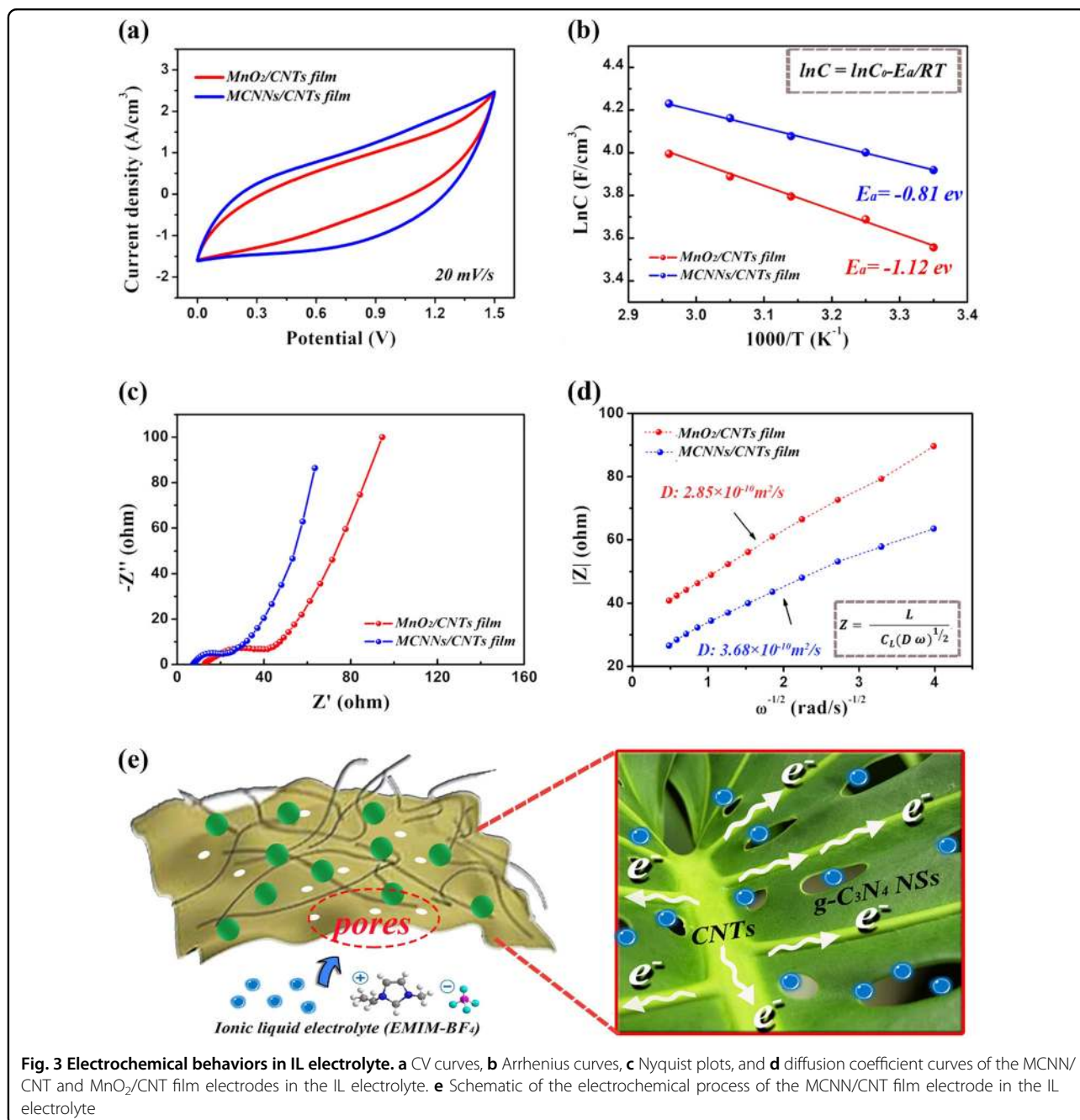
electrode in the IL electrolyte was calculated to be $\sim 0.48 \text{ mJ m}^{-2}$, which was almost four times lower than that of the MnO₂/CNT film electrode (1.86 mJ m^{-2}). The low γ_{sl} value indicated the strong adhesion between the MCNN/CNT film electrode and the IL electrolyte, which was due to the abundant pore channels and active sites of the *g*-C₃N₄ NSs in the MCNN/CNT film electrode (Figs. 2e and S5).

Figure 3a shows the CV curves of the MCNN/CNT and MnO₂/CNT film electrodes in the EMIMBF₄ IL electrolyte, which were obtained using a three-electrode setup. The capacitive performance of the MCNN/CNT film electrode was significantly higher than that of the MnO₂/CNT film electrode, mainly owing to the favorable ionic diffusion of the MCNN/CNT film electrode in the IL electrolyte. To investigate the ionic diffusion of the film electrode in detail, the apparent activation energy, i.e., the energy barrier between the electrode and electrolyte, was calculated using the classical

Arrhenius formula^{36,37}:

$$\ln C = \ln C_0 - E_a/RT, \quad (5)$$

where C is the amount of accumulated charge at the electrode/electrolyte interface, which is the specific capacitance of electrode; C_0 is the pre-exponential constant; E_a is the activation energy; R is the universal gas constant; and T is the absolute temperature. By plotting the values of $\ln C$ with respect to $1/T$, a straight line with a slope of K was obtained, allowing a straightforward calculation of $-E_a$ (eV; $1 \text{ eV} = 0.096 \text{ mJ mol}^{-1}$). Figure 3b shows the corresponding Arrhenius curves of $\ln C$ (C : volumetric specific capacitance at 100 mA cm^{-3}) vs. $1/T$ (T : temperatures ranging from 25 to 65 °C) for the MnO₂/CNT and MCNN/CNT film electrodes in the IL electrolyte. The activation energy of the MCNN/CNT film electrode was $\sim 0.078 \text{ mJ mol}^{-1}$ ($E_a = -K = 0.81 \text{ eV}$), which was



significantly lower than that of the MnO_2/CNT film electrode ($\sim 0.108 \text{ mJ mol}^{-1}$ ($E_a = -K = 1.12 \text{ eV}$)). The lower activation energy of the film electrode in the IL electrolyte represents a significantly smaller obstacle for the IL ions as they migrate from the electrolyte to the interior of the film electrode, leading to the high motion of IL ions in the MCNN/CNT film electrode. As shown in the Nyquist plots (Fig. 3c), the MCNN/CNT film electrode showed superior electrochemical kinetics compared with the MnO_2/CNT film electrode. In addition, the diffusion coefficient of the IL ions in the

MCNN/CNT film electrode was calculated to be $3.68 \times 10^{-10} \text{ m}^2 \text{ s}^{-1}$ (Fig. 3d), which was higher than that in the MnO_2/CNT film electrode ($2.85 \times 10^{-10} \text{ m}^2 \text{ s}^{-1}$), confirming the enhanced IL ion dynamics of the MCNN/CNT film electrode. More calculation details about the diffusion coefficient are shown in Fig. S6. Additional information regarding the electrochemical test results of the MCNN/CNT film electrode is provided in Figs. S7 and S8 and shows its high specific capacitance with good rate and cycle performance in the IL electrolyte.

The excellent electrochemical behavior of the MCNN/CNT film electrode in the IL electrolyte was mainly due to the Monstera leaf-like structure with porous $g\text{-C}_3\text{N}_4$ NSs providing ion-accessible “highway” channels (Fig. 3e). The $g\text{-C}_3\text{N}_4$ NSs with abundant pore channels and reaction sites enhanced the interfacial wettability between the film electrode and the IL electrolyte. The relatively large mesopores of the $g\text{-C}_3\text{N}_4$ NSs offered the IL ions easy access into the film electrode, and the ultrathin wall of the $g\text{-C}_3\text{N}_4$ NSs reduced the inner-pore migration distance of the IL ions. This mechanism was similar to that of the pores in Monstera leaves for the permeation of air and water vapor. Large amounts of IL ions could rapidly diffuse into the interior of the film electrode (blue arrow) to participate in the electrochemical reaction with electroactive MnO_2 nanoparticles. Furthermore, the highly conductive CNTs in the MCNN/CNT film electrode enhanced the charge-transport efficiency (white arrows), mimicking the transfer of organic nutrients through the veins of a leaf. Supplementary Movie 1 shows the ionic diffusion and charge transport in the MCNN/CNT film electrode. According to the foregoing discussion, the superwetable MCNN/CNT film electrode with a unique configuration has high compatibility with the IL electrolyte and remarkably enhances the accommodation of IL ions.

Similar to the IL electrolyte, an ionogel—a solid-state electrolyte—exhibits nonvolatility, nonflammability, high thermal stability, and a wide electrochemical potential window. Hence, FISCs were fabricated with an ionogel electrolyte using a P(VDF-HFP) copolymer as a gelator and hydrophobic EMIMBF₄ IL as a solvent (Fig. 4a). Differentiated by the stable potential ranges in the IL electrolyte (Fig. 4b), the MCNN/CNT film and CCNN/CNT film (Fig. S9) were used as the positive and negative electrodes, respectively, in the device. The asymmetric design ensured that the fabricated FISCs had optimal capacitive performance. The CV curves indicated a high working voltage of 3 V (Fig. 4c), yielding electrochemical behavior significantly better than that of symmetric devices (Fig. S10). Figure 4d shows the galvanostatic charge/discharge (GCD) curves of the devices in the range of 100–800 mA cm⁻³. According to the SEM image, the total volume of the fabricated devices was approximately 0.06 cm³ (Fig. S11). The devices delivered a high volumetric capacitance of 8.6 F cm⁻³ at 100 mA cm⁻³, achieving a maximum volumetric energy density of 10.5 mWh cm⁻³ (Fig. 4e). This energy storage performance is superior to that of previously reported flexible solid-state SCs (mostly <2.5 mWh cm⁻³, Table S1) and several times higher than that of commercially available SCs (2.75 V/44 mF and 5.5 V/100 mF)³⁸. The maximum volumetric power density of the SCs was 1804 mW cm⁻³ at a volumetric energy density of 4.2 mWh cm⁻³, which is

comparable to that of commercially available SCs and significantly higher than that of thin-film lithium-ion batteries. As a result, the FISCs were able to power a motor fan and light a colorful LED (Fig. 4f).

To investigate the electrochemical mechanism of the fabricated FISCs in detail, the surface-reaction contribution and diffusion-controlled contribution of the total capacitance were examined. The linear relationship between the response current and scan rate corresponded to the surface-reaction and diffusion-controlled processes, which are defined by Eqs. (6) and (7)³⁶.

$$i = a \times v^b, \quad (6)$$

$$\ln(i) = \ln(a) + b \times \ln(v). \quad (7)$$

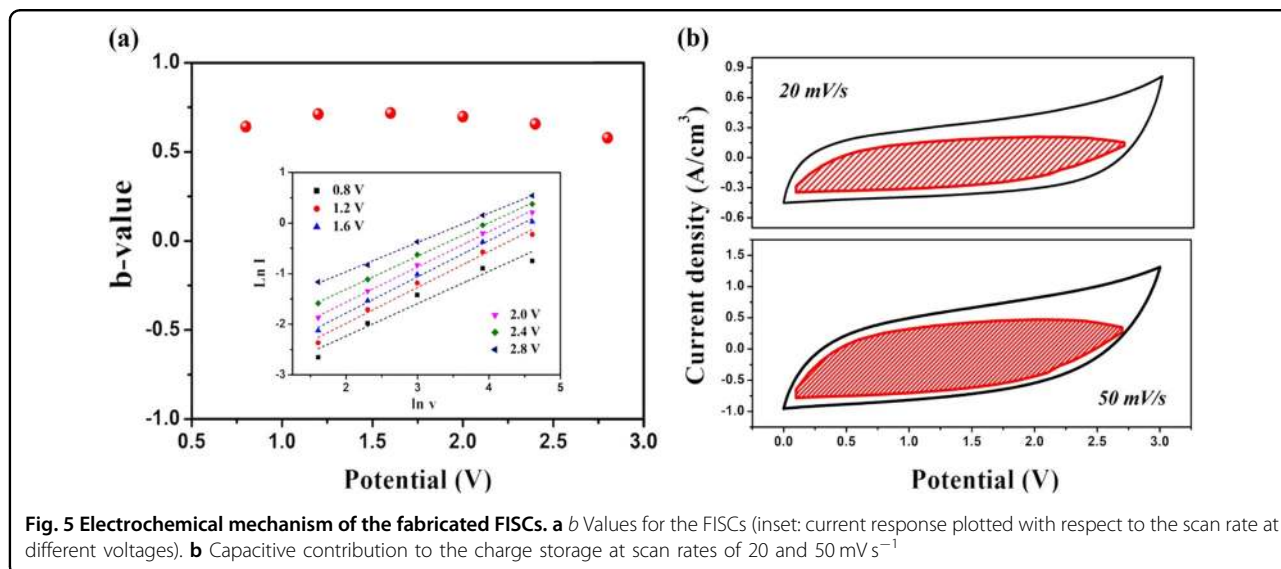
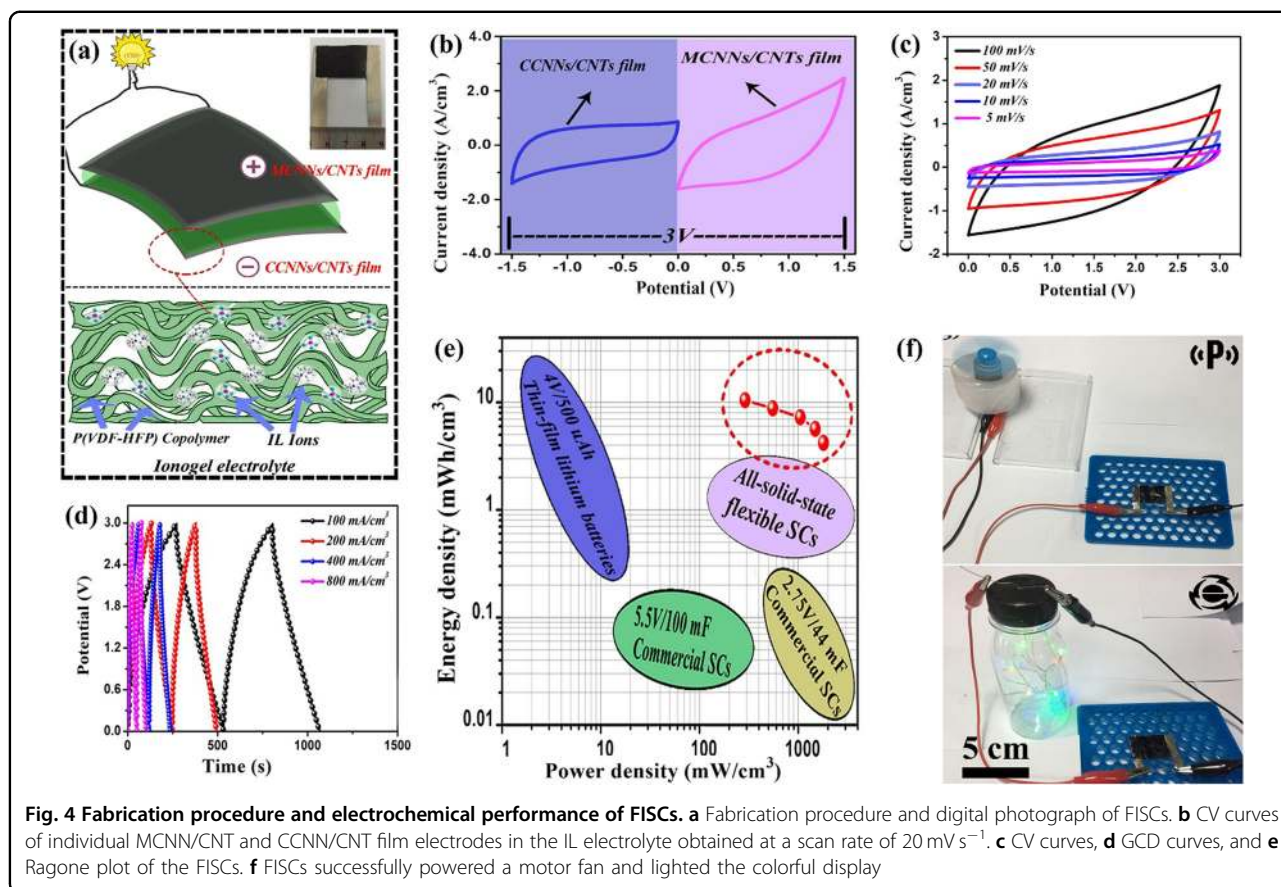
As shown in Fig. 5a, b values were in the range of 0.6–1.0, indicating a coupled diffusion-controlled and capacitive process for storage in the FISCs. The capacitive contribution to the total current was quantified using Eqs. (8) and (9)³⁹:

$$i = k_1 v + k_2 v^{1/2}, \quad (8)$$

$$i/v^{1/2} = k_1 v^{1/2} + k_2. \quad (9)$$

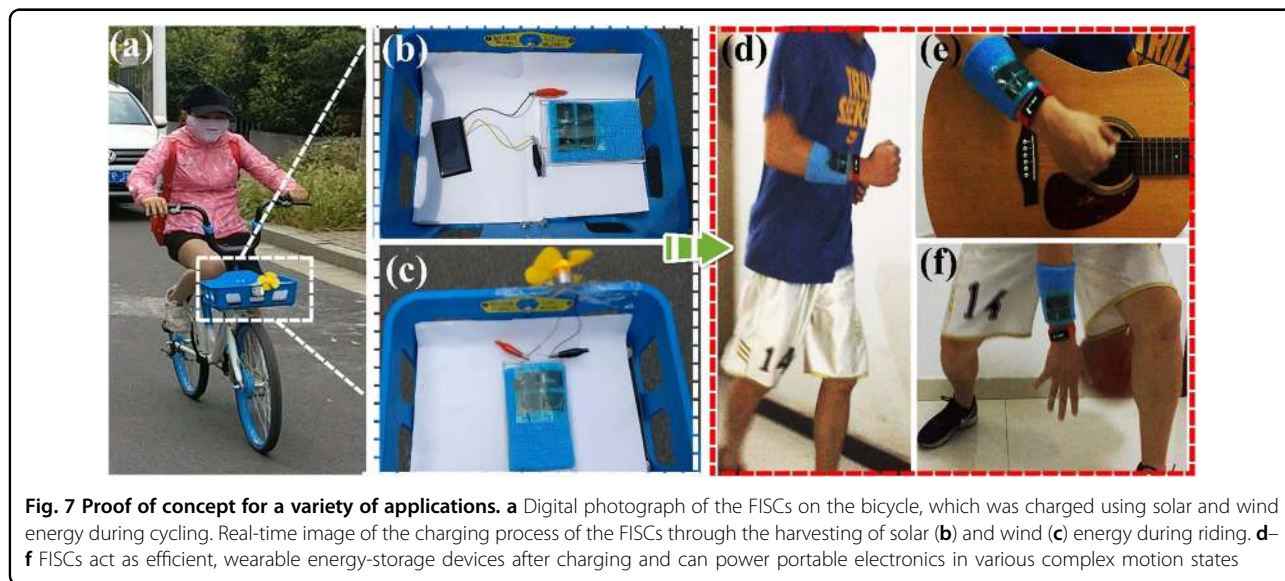
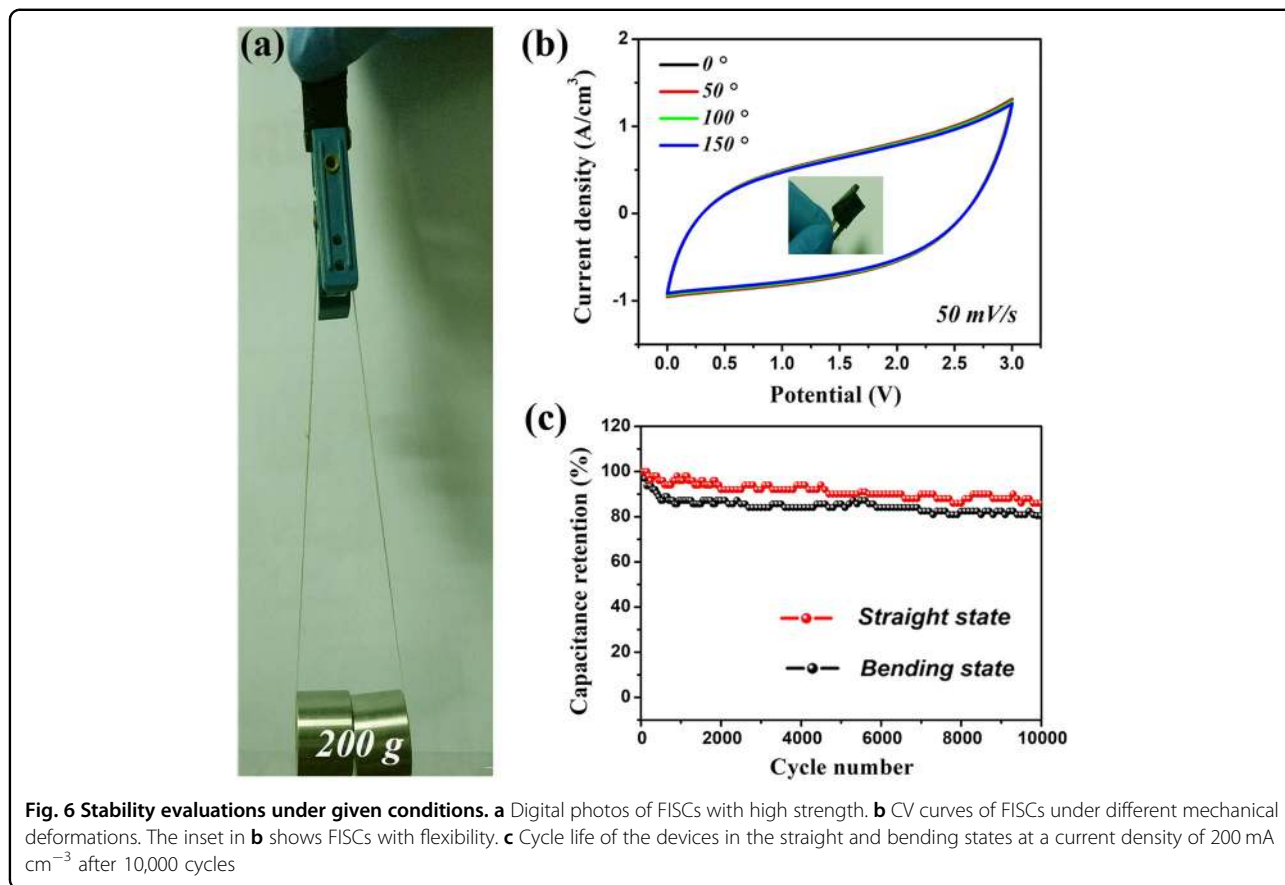
As shown in Fig. 5b, the capacitive contribution to the total current increased from 50.8% at 20 mV s⁻¹ to 65.6% at 50 mV s⁻¹. The results showed that the contribution of the diffusion-limited process to the total capacity was noticeable at scan rates below 20 mV s⁻¹. At scan rates of ≥ 50 mV s⁻¹, the response comprised surface capacitive effects rather than being diffusion controlled, which was beneficial to achieving a high power density at high current densities with the fabricated FISCs.

In addition to their satisfactory electrochemical performance, the FISCs exhibited high strength (Fig. 6a and S12) and flexibility (inset in Fig. 6b). The CV curves of the devices exhibited negligible changes under various conditions (Fig. 6b). The devices maintained nearly 100% of their initial capacitance upon bending at different angles. Under both straight and bending conditions, the FISCs showed strong durability (Fig. 6c), indicating their high electrochemical reliability under harsh mechanical conditions (Fig. S13). The FISCs exhibited a high capacitance retention ratio of 88.5% after 10,000 cycles in the straight state, outperforming previously reported SCs based on an IL or ionogel electrolyte^{36,40}. Owing to their soft and robust structure, the FISCs can be tailored by cutting them into a particular size and shape (Fig. S14). The versatility in the shape of the FISCs gives them potential for a wide range of applications in stylish energy-storage devices.



Energy sustainability is crucial for modern society. For instance, harvesting solar and wind energy can resolve all the present energy concerns and reduce the reliance on fossil fuels. To overcome the intermittency of solar/wind energy, an attempt to store this type of energy in FISCs was made. A commercial miniature solar-cell panel (SCP)

and a wind-driven generator (WDG, Fig. S15) were assembled using the fabricated FISCs as a sustainable energy system. Four FISCs connected in a serial and parallel arrangement (Fig. S16) served as an energy-storage module, collecting solar energy generated by the SCP on sunny days and wind energy generated by the



WDG in windy weather (Fig. S17). After charging, the FISCs could effectively power various portable electronics. The corresponding videos are shown in Supplementary Movies 2 and 3. For a real-world application, the sustainable energy system was directly attached to a

commercial bicycle. The SCP and WDG were placed inside and on the front of the basket of the bicycle, respectively. During riding, the panel of the SCP was completely exposed to the sun, and the blades of the WDG could turn at a high speed under the wind

produced by the motion of the bicycle (Fig. 7a); hence, the FISCs on the bicycle were charged by harvesting solar and wind energy (Fig. 7b, c). More importantly, the FISCs functioned as efficient, wearable energy-storage devices after charging, powering portable electronics in various complex motion states (Fig. 7d–f). The corresponding video is shown in Supplementary Movie 4. To the best of our knowledge, the strategy of developing a sustainable energy system for portable electronics has hardly been exploited, particularly systems utilizing wind power, which is rarely studied. Self-discharging performance is a crucial parameter for the practical application of SCs. As shown in Fig. S19, the fabricated FISCs underwent a rapid self-discharge process in the first few minutes and gradually slowed down after several hours. Finally, the open-circuit voltage of the devices was maintained at ~ 2.5 V beyond 10 h, indicating the low self-discharge rate of the fabricated FISCs after harvesting sustainable energy. Therefore, this study introduces a new avenue for sustainable energy harvesting, as well as wearable and portable energy storage, which are of great significance for practical use of renewable energy resources.

Conclusions

We successfully developed and demonstrated an innovative methodology for preparing a bioinspired *Monstera* leaf-like MCNN/CNT film electrode. Similar to the pores in *Monstera* leaves for the permeation of air and water vapor, the film electrode was based on porous $g\text{-C}_3\text{N}_4$ NSs as ion-accessible channels, leading to the ultrafast spreading of IL ions. According to detailed investigations and accurate calculations, the film electrode exhibited extraordinary ion dynamics and superior wettability in an IL electrolyte. Using the CCNN/CNT film electrode, tailorable FISCs were fabricated that exhibited a high energy/power density and excellent rate and cycle capability. FISCs can be charged by harvesting solar/wind energy and can effectively power various portable electronics. The versatility in the shape of the tailorable FISCs makes them suitable for a wide range of applications in stylish energy-storage devices. Considering the facile fabrication and outstanding performance of the developed electrode, this study paved the way for the integration of sustainable energy harvesting and flexible energy storage.

Acknowledgements

Minjie Shi and Cheng Yang contributed equally to this work. We appreciate the fruitful discussions with Prof. François Béguin at Poznan University of Technology and Dr. Qiang Gao at Oak Ridge National Laboratory. We greatly acknowledge the funding for this project through the National Natural Science Foundations of China (No. 51873083), the Opening Project of State Key Laboratory of Polymer Materials Engineering (Sichuan University) (No. sklpm2018-4-27), the Six Talent Peaks Project in Jiangsu Province (No. 2015-XCL-028), the Postgraduate Research & Practice Innovation Program of Jiangsu

Province (KYCX17_1831, SJCX18_0759), the Key University Science Research Project of Jiangsu Province (18KJA130001), and the Beijing Natural Science Foundation (No. 2192039). J.-H.A. acknowledges support from the National Research Foundation of Korea (NRF-2015R1A3A2066337). Z.S. acknowledges support from National Natural Science Foundation of China (NSFC, No. 21972010) and Beijing Natural Science Foundation (No. 2192039).

Author details

¹School of Materials Science and Engineering, Jiangsu University of Science and Technology, 212003 Zhenjiang, China. ²State Key Laboratory of Organic-Inorganic Composites, Beijing University of Chemical Technology, 100029 Beijing, China. ³Integrated Composites Lab (ICL), Department of Chemical & Biomolecular Engineering, University of Tennessee, Knoxville, TN 37996, USA. ⁴School of Electrical & Electronic Engineering, Yonsei University, Seoul 03722, Republic of Korea

Conflict of interest

The authors declare that they have no conflict of interest.

Publisher's note

Springer Nature remains neutral with regard to jurisdictional claims in published maps and institutional affiliations.

Supplementary information is available for this paper at <https://doi.org/10.1038/s41427-019-0161-7>.

Received: 15 June 2019 Revised: 28 July 2019 Accepted: 30 July 2019.
Published online: 25 October 2019

References

- Dubal, D. P., Chodankar, N. R., Kim, D. H. & Gomez-Romero, P. Towards flexible solid-state supercapacitors for smart and wearable electronics. *Chem. Soc. Rev.* **47**, 2065–2129 (2018).
- Cai, X. K., Luo, Y. T., Liu, B. & Cheng, H. M. Preparation of 2D material dispersions and their applications. *Chem. Soc. Rev.* **47**, 6224–6266 (2018).
- Yang, B. C. et al. Flexible black-phosphorus nanoflake/carbon nanotube composite paper for high-performance all-solid-state supercapacitors. *ACS Appl. Mater. Interfaces* **9**, 44478–44484 (2017).
- Li, Q. W. et al. Spatially confined synthesis of vanadium nitride nanodots intercalated carbon nanosheets with ultrahigh volumetric capacitance and long life for flexible supercapacitors. *Nano Energy* **51**, 128–136 (2018).
- Yu, L. Y. et al. MXene-bonded activated carbon as a flexible electrode for high-performance supercapacitors. *ACS Energy Lett.* **3**, 1597–1603 (2018).
- Lai, F. L. et al. Breaking the limits of ionic liquid-based supercapacitors: mesoporous carbon electrodes functionalized with manganese oxide nanosplatches for dense, stable, and wide-temperature energy storage. *Adv. Funct. Mater.* **28**, 1801298 (2018).
- Li, J. et al. Interactions between graphene and ionic liquid electrolyte in supercapacitors. *Electrochim. Acta* **197**, 84–91 (2016).
- Simotwo, S. K., Chinnam, P. R., Wunder, S. L. & Kalra, V. Highly durable, self-standing solid-state supercapacitor based on an ionic liquid-rich ionogel and porous carbon nanofiber electrodes. *ACS Appl. Mater. Interfaces* **9**, 33749–33757 (2017).
- Feng, L. X. et al. Flexible solid-state supercapacitors with enhanced performance from hierarchically graphene nanocomposite electrodes and ionic liquid incorporated gel polymer electrolyte. *Adv. Funct. Mater.* **28**, 1704463 (2018).
- Li, J., Wang, N., Tian, J. R., Qian, W. Z. & Chu, W. Cross-coupled macro-mesoporous carbon network toward record high energy-power density supercapacitor at 4 V. *Adv. Funct. Mater.* **28**, 1870360 (2018).
- Yan, R. Y., Antonietti, M. & Oschatz, M. Toward the experimental understanding of the energy storage mechanism and ion dynamics in ionic liquid based supercapacitors. *Adv. Energy Mater.* **8**, 1800026 (2018).
- Peng, L. L., Fang, Z. W., Zhu, Y., Yan, C. S. & Yu, G. H. Holey 2D nanomaterials for electrochemical energy storage. *Adv. Energy Mater.* **8**, 1702179 (2018).

13. Guo, F. et al. Facile bottom-up preparation of Cl-doped porous g-C₃N₄ nanosheets for enhanced photocatalytic degradation of tetracycline under visible light. *Sep. Purif. Technol.* **228**, 115770 (2019).
14. Xiao, Y. T. et al. Molecule self-assembly synthesis of porous few-layer carbon nitride for highly efficient photoredox catalysis. *J. Am. Chem. Soc.* **141**, 2508–2515 (2019).
15. Guo, F. et al. 2D/2D Z-scheme heterojunction of CuInS₂/g-C₃N₄ for enhanced visible-light-driven photocatalytic activity towards the degradation of tetracycline. *Sep. Purif. Technol.* **210**, 608–615 (2019).
16. Yang, L. Q. et al. A surface modification resultant thermally oxidized porous g-C₃N₄ with enhanced photocatalytic hydrogen production. *Appl. Catal. B* **204**, 335–345 (2017).
17. Li, X. D. et al. Smart hybrids of Zn₂GeO₄ nanoparticles and ultrathin g-C₃N₄ layers: synergistic lithium storage and excellent electrochemical performance. *Adv. Funct. Mater.* **25**, 6858–6866 (2015).
18. Han, M. N. et al. Efficient bifunctional Co/N dual-doped carbon electrocatalysts for oxygen reduction and evolution reaction. *Carbon* **153**, 575–584 (2019).
19. Dong, B. T. et al. Formation of g-C₃N₄@Ni(OH)₂ honeycomb nanostructure and asymmetric supercapacitor with high energy and power density. *ACS Appl. Mater. Interfaces* **9**, 17890–17896 (2017).
20. Li, Z. C., Wu, L., Wang, L. B., Gu, A. J. & Zhou, Q. F. Nickel cobalt sulfide nanosheets uniformly anchored on porous graphitic carbon nitride for supercapacitors with high cycling performance. *Electrochim. Acta* **231**, 617–625 (2017).
21. Zhang, L. et al. Enhanced supercapacitive performance of graphite-like C₃N₄ assembled with NiAl-layered double hydroxide. *Electrochim. Acta* **186**, 292–301 (2015).
22. Zhao, Y. et al. Facile preparation of TiO₂/C₃N₄ hybrid materials with enhanced capacitive properties for high performance supercapacitors. *J. Alloys Compd.* **702**, 178–185 (2017).
23. Duan, J. J., Chen, S., Jaroniec, M. & Qiao, S. Z. Porous C₃N₄ nanolayers@N-graphene films as catalyst electrodes for highly efficient hydrogen evolution. *ACS Nano* **9**, 931–940 (2015).
24. Zang, X. B. et al. Flexible, temperature-tolerant supercapacitor based on hybrid carbon film electrodes. *Nano Energy* **40**, 224–232 (2017).
25. Zhang, L., Huang, Y., Zhang, Y., Fan, W. & Liu, T. Three-dimensional nanoporous graphene-carbon nanotube hybrid frameworks for confinement of SnS₂ nanosheets: flexible and binder-free Papers with highly reversible lithium storage. *ACS Appl. Mater. Interfaces* **7**, 27823–27830 (2015).
26. Xu, C. et al. Interweaving metal-organic framework-templated Co-Ni layered double hydroxide nanocages with nanocellulose and carbon nanotubes to make flexible and foldable electrodes for energy storage devices. *J. Mater. Chem. A* **6**, 24050–24057 (2018).
27. Christoforidis, K. C. et al. Metal-free dual-phase full organic carbon nanotubes/g-C₃N₄ heteroarchitectures for photocatalytic hydrogen production. *Nano Energy* **50**, 468–478 (2018).
28. Jin, Y., Chen, H., Chen, M., Liu, N. & Li, Q. Graphene-patched CNT/MnO₂ nanocomposite papers for the electrode of high-performance flexible asymmetric supercapacitors. *ACS Appl. Mater. Interfaces* **5**, 3408–3416 (2013).
29. Ma, T. Y., Dai, S., Jaroniec, M. & Qiao, S. Z. Graphitic carbon nitride nanosheet-carbon nanotube three-dimensional porous composites as high-performance oxygen evolution electrocatalysts. *Angew. Chem. Int. Ed. Engl.* **53**, 7281–7285 (2014).
30. Liu, Q. & Zhang, J. Y. Graphene supported Co-g-C₃N₄ as a novel metal-macrocyclic electrocatalyst for the oxygen reduction reaction in fuel cells. *Langmuir* **29**, 3821–3828 (2013).
31. Xu, J., Zhang, R., Chen, P. & Ge, S. Effects of adding ethanol to KOH electrolyte on electrochemical performance of titanium carbide-derived carbon. *J. Power Sources* **246**, 132–140 (2014).
32. Xu, J. et al. Electrochemical performance of graphitized carbide-derived-carbon with hierarchical micro- and meso-pores in alkaline electrolyte. *Carbon* **74**, 226–236 (2014).
33. Zhang, J. et al. Fabrication of Novel ternary three-dimensional RuO₂/graphitic-C₃N₄@reduced graphene oxide aerogel composites for supercapacitors. *ACS Sustain. Chem. Eng.* **5**, 4982–4991 (2017).
34. Bellanger, H., Darmanin, T., Taffin de Givenchy, E. & Guittard, F. Chemical and physical pathways for the preparation of superoleophobic surfaces and related wetting theories. *Chem. Rev.* **114**, 2694–2716 (2014).
35. Su, B., Tian, Y. & Jiang, L. Bioinspired interfaces with superwettability: from materials to chemistry. *J. Am. Chem. Soc.* **138**, 1727–1748 (2016).
36. Shen, B. S. et al. A high-temperature flexible supercapacitor based on pseudocapacitive behavior of FeOOH in an ionic liquid electrolyte. *J. Mater. Chem. A* **4**, 8316–8327 (2016).
37. Ujjain, S. K., Sahu, V., Sharma, R. K. & Singh, G. High performance, all solid state, flexible supercapacitor based on ionic liquid functionalized graphene. *Electrochim. Acta* **157**, 245–251 (2015).
38. Chen, J. Z., Fang, K. L., Chen, Q. Y., Xu, J. L. & Wong, C. P. Integrated paper electrodes derived from cotton stalks for high-performance flexible supercapacitors. *Nano Energy* **53**, 337–344 (2018).
39. Zhou, J. et al. A conductive and highly deformable all-pseudocapacitive composite paper as supercapacitor electrode with improved areal and volumetric capacitance. *Small* **14**, 1803786 (2018).
40. Pandey, G. P. & Hashmi, S. A. Performance of solid-state supercapacitors with ionic liquid 1-ethyl-3-methylimidazolium tris(pentafluoroethyl) trifluorophosphate based gel polymer electrolyte and modified MWCNT electrodes. *Electrochim. Acta* **105**, 333–341 (2013).